World Scientific
www.worldscientific.com

In vivo mice brain microcirculation monitoring based on contrast-enhanced SD-OCT

Shaozhuang Yang*, Liwei Liu*,‡,¶, Yixin Chang†, Ningning Zhang†, Kun Liu†,
Liang Hong*, Bingling Chen*, Yue Zhao*, Rui Hu* and Junle Qu*,§,¶

*Key Laboratory of Optoelectronic Devices and Systems
of Ministry of Education and Guangdong Province
Shenzhen University, Shenzhen 518060, P. R. China*

†*State Key Laboratory of Supramolecular Structure and Materials
Jilin University, Changchun 130012, P. R. China*
‡*liulw@szu.edu.cn*
§*jlqu@szu.edu.cn*

In this paper, we proposed a contrast-enhanced homemade spectral domain optical coherence tomography (SD-OCT) method for monitoring of brain microcirculation. We used the polyethylene glycol (PEG)-ylated gold nanorods (GNRs) as a contrast-enhanced agent, obtained clearly 2D and 3D OCT images of blood vessels and dynamic changes of probes in mouse blood vessels. Owing to high scattering of the PEG-GNRs, more tiny blood vessels can be imaged and the OCT signal can be enhanced by 5.87 dB after injection of PEG-GNRs for 20 min, the enhancement then declined gradually for 60 min. Our results demonstrate an effective technique for the enhanced imaging of blood vessels *in vivo*, especially for studies of the brain microcirculation, which could be serviced for disease mechanism research and therapeutic drug monitoring.

Keywords: Optical coherence tomography; brain microcirculation; cerebral blood vessels; gold nanorods.

1. Introduction

Blood circulation plays an important role in regulating metabolism and immune function in tissues, so the physiological state of blood circulation can reflect the health status of biological tissues or organs. Clinically, angiography can provide an effective diagnostic basis for disease diagnosis. Cerebral vascular structure, distribution and cerebral blood

¶Corresponding authors.

flow and other parameters are closely related to cerebrovascular diseases and are important indicators of cerebral vascular diseases.[1,2] Therefore, the imaging and monitoring of brain microcirculation has important research significance for the detection and diagnosis of brain diseases.

Optical coherence tomography (OCT) is one of the most promising new tomographic imaging techniques, especially in clinical diagnosis it has an attractive application prospect. Recently, OCT technique has been widely applied in monitoring brain microcirculation[3–6] because of its high-imaging depth, high-resolution and rapid 3D *in vivo* imaging ability. However, the penetration depth and contrast decrease sharply in highly scattering tissues, thereby limiting further extensions of the method and applications for clinical diagnosis.

In the meanwhile, the emergence of new multifunctional nanomaterials has promoted the development and application of optical imaging contrast agents. The functional materials,including NIR dyes,[7] phytochrome A,[8] branched gold nanoparticles,[9] and gold nanorings,[10] etc., have been developed and implemented *in vitro* to enhance OCT signal and image contrast, which provide a very good reference for the research of contrast-enhanced OCT imaging *in vivo*. Particularly worth mentioning is that some scientists had developed new materials such as Intralipid,[11] large gold nanorods,[12] gold nanoshells,[13] microspheres[14] and microbubbles,[15] which had been successfully applied and verified in mouse and human blood flow models. Using these functional materials as contrast agents, the high resolution and high contrast OCT images of microvascular and blood flow can be obtained, which greatly promote the development of OCT angiography and expand its application.

Among various functional materials that are under active investigation for biomedical applications, gold nanorods (GNRs) have attracted increasing attention as efficient tags for various diagnostic and therapeutic agents, primarily owing to their special optical characteristics.[16,17] On the one hand, the synthesis process of GNRs was simpler and more mature than other materials. At the same time, GNRs have lower biotoxicity and better biocompatibility. On the other hand, GNRs are characterized by strong scattering cross-sections and can be used to enhance the signal intensity and contrast of OCT images,[18–21] which helps to improve the imaging capability of OCT and provide

more detailed detection information for cerebral blood vessels, especially for brain microcirculation.

In this study, we presented an SD-OCT measurement for monitoring of brain microcirculation. we prepared (polyethylene glycol)ylated GNRs (PEG-GNRs) with average dimensions of 30.42 ± 2.00 nm (length) $\times 5.51 \pm 0.40$ nm (diameter) and an aspect ratio of 5.5 to be as contrast agent for OCT detection. By PEG-GNRs contrast-enhanced SD-OCT, the clear brain microvascular flow had been obtained and image contrast increased by 5.87 dB. We also got the clearly 3D imaging of the cerebral blood vessels, by improving the algorithm. These results indicated that contrast-enhanced SD-OCT can achieve the functional imaging and monitoring of brain microcirculation and brain ischemia, which provided a valuable method for the effective detection of cerebrovascular disease in clinical diagnosis.

2. Materials and Methods

2.1. Synthesis of GNRs

All chemicals for PEG-GNRs synthesis were purchased from Sigma-Aldrich (St. Louis, MO, USA), unless otherwise indicated. GNRs were synthesized by the seed-mediated growth method as reported previously.[22,23] The seed solution was prepared by mixing chloroauric acid ($HAuCl_4$) (0.12 mL, 15 mM) with an aqueous solution of hexadecyltrimethylammonium bromide (CTAB) (2.5 mL, 0.20 M), 1.0 mL of deionized water, and a freshly prepared, ice-cold sodium borohydride ($NaBH_4$) solution (0.50 mL, 10 mM) at 25.5°C. The mixture was stirred for 120 s. The seeds could be used within 0.5–2 h when stored in a 25°C bath. To prepare the growth solution, 0.3645 g of CTAB was dissolved in 8.876 mL of deionized water. The CTAB solution was mixed with an aqueous solution of silver nitrate ($AgNO_3$) (0.40 mL, 4.0 mM) and $HAuCl_4$ (0.50 mL, 15 mM). The color of the solution changed from dark yellow to colorless after the addition of ascorbic acid (0.124 mL, 0.788 M). Finally, 0.10 mL of a 30-min-aged seed solution was added to the growth solution and incubated at 27°C for at least 20–24 h.

2.2. Preparation of PEG-GNRs

The as-prepared GNRs (1.0 mL, 0.8 nM) were purified by centrifugation at 13011 g for 15 min and

re-dispersed in the same volume of deionized water. After the addition of Thiolated-PEG (HS-PEG) (0.10 mL, 0.20 mM), the solution was vortexed immediately and incubated for over 12 h at room temperature. Finally, the PEG-GNRs were centrifuged at 13011 g for 15 min to remove excess HS-PEG. The average size of the PEG-GNRs was determined by measuring the length and width of all the 79 intact rods in the inset of Fig. 4(a) and calculating the average and standard deviation.

2.3. *Analysis of cell viability*

We used breast cancer cells to evaluate the cytocompatibility of PEG-GNRs according to the literature.[24] MCF-7 breast cancer cells were cultured in DMEM supplemented with 10% fetal bovine serum (FBS; Hyclone, Logan, UT, USA), penicillin (100 U/mL; Gibco, Grand Island, NY, USA), and streptomycin (100 μg/mL, Gibco) at 37°C with 5% CO_2. The cell viability of MCF-7 with PEG-GNRs was examined by MTT (3-(4,5-dimethylthiazol-2-yl)-2,5-diphenyltetrazolium bromide; Life Technologies, Carlsbad, CA, USA) assays. Cancer cells seeded in 96-well plates were incubated with control (DMEM medium) or PEG-GNR solutions at various concentrations (0.1, 0.2, 0.4, 0.6, and 0.8 nM) for 48 h. Then, 20 μL of MTT solution was added to each well to reach an ultimate concentration of 0.5 mg/mL. After another 4 h of incubation, the solution in each well was removed and the purple precipitate was dispersed in 150 μL of dimethyl sulfoxide (DMSO; Alfa, Montgomery, AL, USA). The absorbance of the solution in the wells was measured using a TECAN M200 Pro Microplate Reader (Männedorf, Switzerland) at a wavelength of 495 nm. Cell viability was calculated by normalizing the absorbance of the sample wells to that of the control wells. Experiments were performed in triplicate. The data were subjected to statistical analysis using software SPSS 16.0. All the data were reported as mean values ± standard deviations (SD). One-way analysis of variance (ANOVA) followed by Levene's Test for equality of variances as well as Bonferroni multiple comparison test was used for the comparison of the mean values. Differences were regarded as significant at $p < 0.05$.

2.4. *Preparation of mouse model*

To examine the effect of PEG-GNRs on cerebral blood vessels *in vivo*, a mouse model of craniotomy
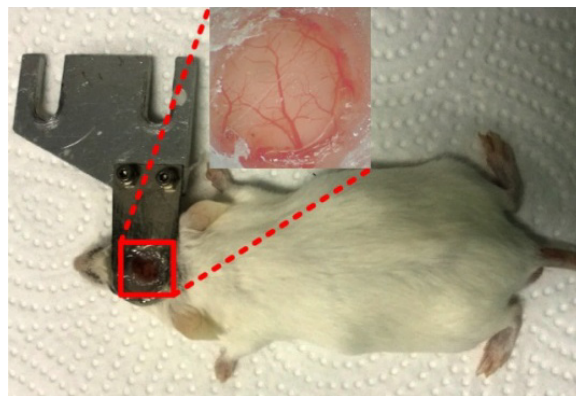

Fig. 1.   Model of mouse craniotomy.

was established. All BALB/c mice used in the experiment were 8 weeks old and weighed about 25 g; mice were purchased from Guangdong Medical Laboratory Animal Center. Additionally, all animal procedures were performed in strict compliance with the requirements and guidelines of the Laboratory and Equipment Department and Institutional Ethical Committee of Animal Experimentation of Health Science Center, Shenzhen University. The anesthetic was administered at 40 mg/kg body weight based on previous results[25]; BALB/c mice were anesthetized by intraperitoneal injections of 100 μL of 1% pentobarbital sodium solution. Under a microscope, each mouse was placed on a 37°C heating pad to remove part of the left rear skull and then a full craniotomy was conducted. A complete image of a mouse model of craniotomy is shown in Fig. 1.

3. SD-OCT System

3.1. *Experimental setup*

We setup an OCT experimental system, this system was developed in previous studies by our group.[26–28] The light source for SD-OCT was superluminescent diode (SLD) with a center wavelength of 835 nm, bandwidth of 45 nm, and power of 12 mW. After optimization and improvement, the transverse resolution, axial resolution and imaging depth (in air) were 6.13 μm, 6.84 μm and 3.62 mm, respectively, and the line rate reached 140 kHz. Hence, it was worth noting that the system exhibited favorable sensitivity and imaging speed, which was suitable for imaging *in vivo*. A schematic diagram of SD-OCT is shown in Fig. 2. According to the imaging
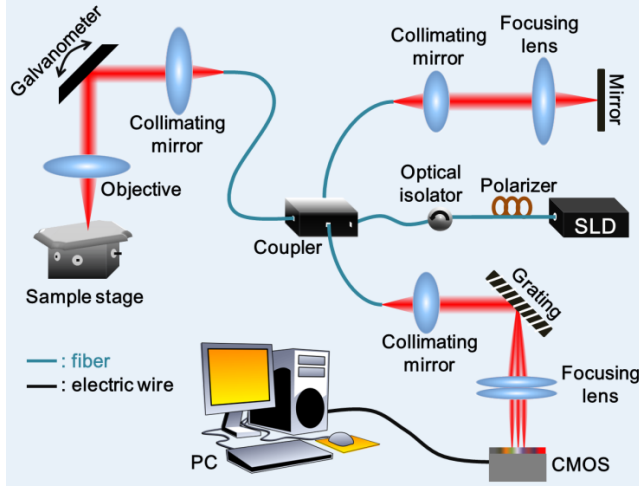
Fig. 2. Schematic diagram of the SD-OCT system.

principle of SD-OCT,[29] the OCT images were obtained by reconstructing the intensity and phase information of backscattered light from sample collection. Therefore, it was credible to characterize the intensity of OCT imaging signal in terms of grayscale intensity.[18,30–32] In this paper, we used this method to measure the intensity of OCT signals in all 2D and 3D OCT images.

3.2. Theoretical analysis of contrast-enhanced SD-OCT

According to the principles of SD-OCT imaging and signal processing,[29] we assumed $a(z)$ was the backward scattering amplitude of the sample at depth z, and the interferential spectral signal of OCT can be expressed by Eq. (1) as follows:

$$I(k) = S(k)\left| a_R e^{i2kr} + \int_0^\infty a(z)e^{i2kz}dz \right|^2, \quad (1)$$

where k is the number of light waves, defined as $k = 2\pi/\lambda$ (with λ equal to the wavelength of the light source). $S(k)$ and a_R represent the power spectral density and the reflection coefficient of reference arm, respectively. The parameters r and z are the optical distances from the same reference plane to the reference and sample arms, respectively. As a general rule, $a_R = 1$, $r = 0$; accordingly, Eq. (1) can be expressed as follows:

$$
\begin{aligned}
I(k) &= S(k)\left| 1 + \int_0^\infty a(z)e^{i2kz}dz \right|^2 \\
&= S(k)\left(1 + \int_0^\infty a(z)e^{i2kz}dz\right)\left(1 + \int_0^\infty a(z)e^{-i2kz}dz\right) \\
&= S(k)(1 + A(k))(1 + A^*(k)) \\
&= S(k)(1 + (A(k) + A^*(k)) + A(k)A^*(k)), \quad (2)
\end{aligned}
$$

where, $A(k) = \int_0^\infty a(z)e^{i2kz}dz$ and $A^*(k) = \int_0^\infty a(z)e^{-i2kz}dz$. The first term $S(k)$ and third term $S(k)A(k)A^*(k)$ are the direct current and autocorrelation items, respectively, and have little effect on $I(k)$. $A^*(k)$ is the Fourier transformation of $a(-z)$, which is the mirroring of SD-OCT image and can be controlled in the imaging process. The OCT signal $I(k)$ is highly dependent on $A(k)$, and there are related according to Eq. (3):

$$I(k) \propto A(k) \propto a(z). \quad (3)$$

3.3. Image processing by BM3D

In the OCT imaging process, some noise was unavoidable, including scanning noise, electronic noise and speckle noise, which seriously affected the imaging quality and information reading. Based on the principle of the maximum retention of image information, the 2D OCT image of skin were denoised
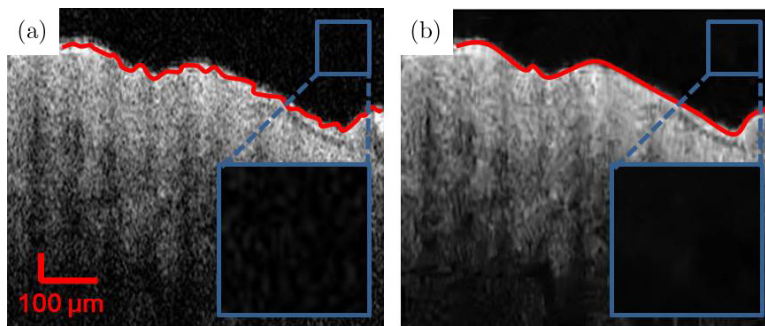

Fig. 3. 2D OCT image of skin before (a) and after (b) denoising by BM3D. (The margins of skin images were marked by red solid lines, and the background noise in ROIs were marked by blue solid rectangles).

using the block-matching 3D (BM3D) algorithm which was programmed by MATLAB.[33] As shown in Fig. 3, the normal skin of human arm was used as a biological sample and the 2D OCT image was obtained. (Note: The arm was directly placed on the sample stage for imaging.) Then, the original image was processed by BM3D. Compared with the original image, we can find that the margins of skin image (marked by red solid lines) became smooth and background noise (marked by blue solid rectangles) decreased after denoising, and its signal-to-noise ratio (SNR) was significantly improved. Therefore, we used this algorithm to optimize the obtained images information.

4. Results and Discussion

4.1. *Characterization of PEG-GNRs*

As shown in Fig. 4(a), the extinction spectrum of PEG-GNRs was recorded using a Shimadzu UV-2550 spectrophotometer with a 1 cm quartz cuvette. The extinction peak was located at 836 nm. TEM images of PEG-GNRs were obtained using a transmission electron microscope (H-600; Hitachi, Tokyo, Japan). The average dimension of PEG-GNRs was $30.42 \pm 2.00\,\text{nm} \times 5.51 \pm 0.40\,\text{nm}$, as shown in the inset of Fig. 4(a).

4.2. *Cell viability using PEG-GNRs*

To examine the biotoxicity of PEG-GNRs, we examined cell viability using MCF-7 breast cancer cells. Various concentrations of PEG-GNRs were applied and MTT assays were performed after 48 h. As shown in Fig. 4(b), no significant alteration of cell viability could be detected in the range of 0–0.8 nM ($p > 0.05$). These results suggested that the probe had low toxicity and good biocompatibility and accordingly was a promising material for biological applications.

4.3. *OCT imaging in vitro*

As we know, PEG-GNRs have strong scattering cross sections, according to the theory of OCT imaging detection, which can enhance in OCT imaging. Based on this property, PEG-GNRs were suitable contrast agents to enhance the signal in OCT imaging detection. In order to evaluate the efficiency of PEG-GNRs as contrast agent for OCT imaging, we used 1% agar with different concentrations of PEG-GNRs as biological tissue phantom to perform experiment *in vitro*. All the production process of agar model was the same as previously reported,[28] and the volume ratio of agar to PEG-GNRs was 2:1. The agar tissue phantoms with and without PEG-GNRs were showed in Fig. 5(A). Then, the above-prepared agar models were placed on operating platform of OCT system for imaging and 2D OCT images were showed in Fig. 5(B). Besides, by measuring and extracting OCT signal of the regions of interest (ROIs) in the 2D OCT images (red solid rectangles in the figures), the attenuation curves were obtained, as shown in Fig. 5(C). Combined with the 2D OCT images of the agar model and the corresponding OCT signal attenuation curves, it can be seen that the agar models mixed with PEG-GNRs had a significantly enhanced OCT signal and increased with increasing concentration of PEG-GNRs, which indicated that PEG-GNRs was a paragon contrast agent for enhanced OCT imaging.
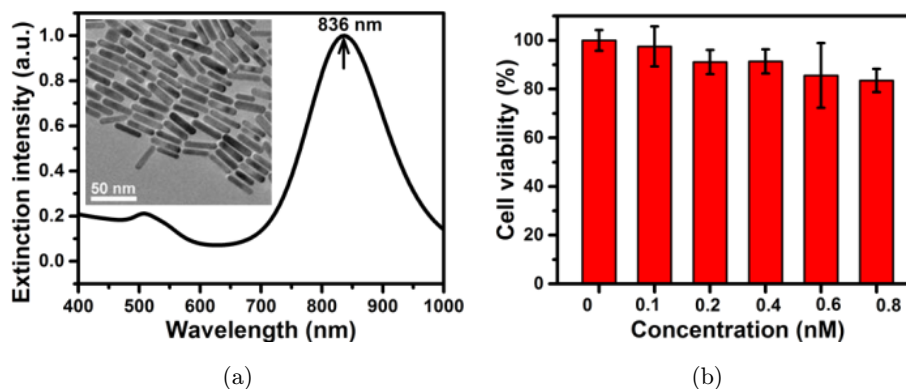

Fig. 4.   (a) Extinction spectrum of PEG-GNRs and TEM image (inset) and (b) Cytotoxicity analysis of PEG-GNRs.
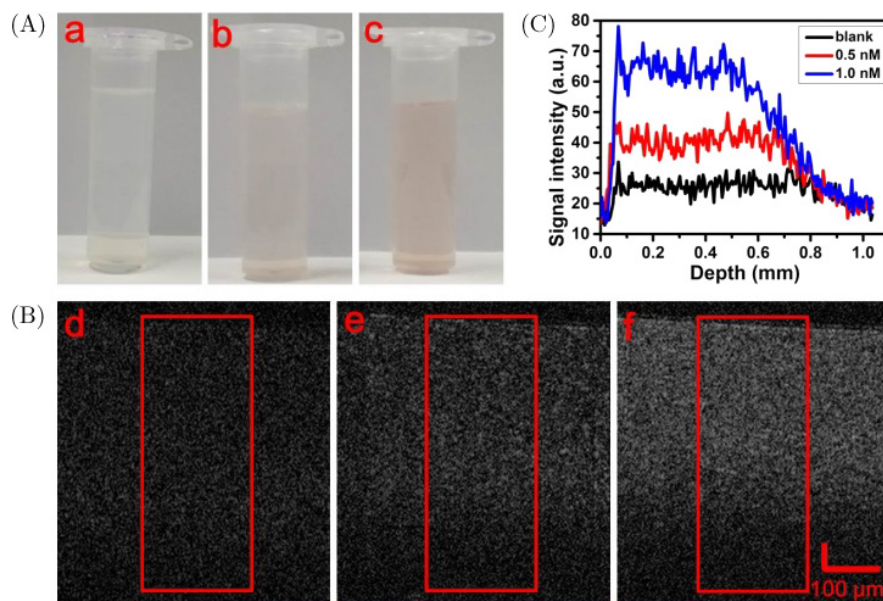
Fig. 5.   (A) Photograph of agar in the absence (a) and presence of different concentrations of PEG-GNRs tissue phantom, i.e., (b) 0.5 nM, (c) 1.0 nM; (B) 2D OCT images in the absence (d) and presence of different concentrations of PEG-GNRs, i.e., (e) 0.5 nM and (f) 1.0 nM; (C) Attenuation curves of OCT signal of ROIs in (B).

4.4.   *OCT imaging in vivo*

Then, we examined (PEG-GNRs)-enhanced OCT imaging of brain blood vessels in mice for imaging and monitoring brain microcirculation, the fundamental goal of our research. We injected $150\,\mu$L of 1 nM PEG-GNRs into mice via the vein tail, which was expected to have high imaging efficiency. Images of mouse cerebral blood vessels were obtained at 5, 10, 15, 20, 25, 40 and 60 min after the injection of PEG-GNRs. In addition, in order to exclude the adverse impact of individual differences of mice in the experiment, all the experimental results were obtained in the same mouse. (*Note*: Throughout the entire experiment, plus errors in the preparation of mouse models and unexpected phenomena in the experiment, a total of 10 mice were used.) According to the 2D OCT images of cerebral blood vessels, the actual imaging depth in the brain of mice craniotomy was about $520\,\mu$m. To quantitatively analyze the effect of PEG-GNR on blood vessels detection in OCT imaging, we selected ROIs and fitted attenuation curves of the OCT signal. The curves were fitted by a 5th-degree polynomial, and relative factors R^2 for all of the curves were greater than 0.95, indicating a good fit. The 2D OCT images of blood vessels and attenuation curves were shown in Fig. 6. Due to the flow and excretion of PEG-GNRs in mouse blood vessels, there were
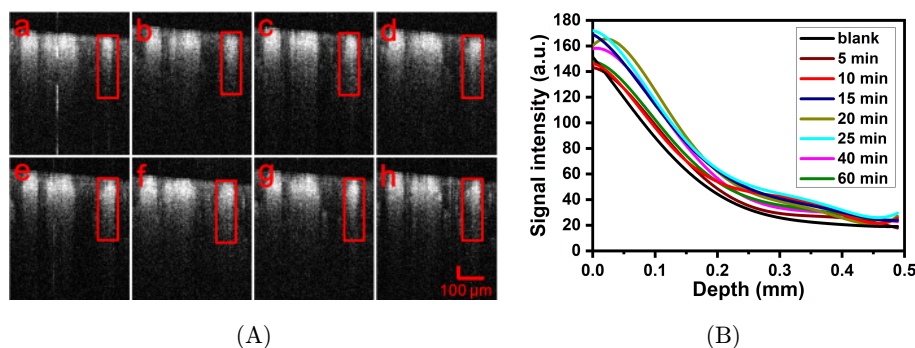

Fig. 6.   (A) 2D OCT images of cerebral blood vessels in mice in the absence (a) and presence of PEG-GNRs (1 nM) at various time points, i.e., (b) 5, (c) 10, (d) 15, (e) 20 (f) 25, (g) 40, and (h) 60 min; (B) Fitted attenuation curves of the OCT signal. (The ROIs marked by red solid rectangles indicate cross-sections of blood vessels).

dynamic changes in the effect of PEG-GNRs in blood vessels whereby the effect increased until 20 min and subsequently decreased. According to the difference of signal attenuation trend at various time points, the role of PEG-GNRs in improving OCT imaging signal was obvious.

During the imaging process, the noise generated by the heartbeat of the mouse caused blurring of the edge of the blood vessel image, which was not conducive to 3D image reconstruction. Here, based on BM3D, all the 2D OCT images of blood vessels had been processed to improve the SNR of images, as shown in Fig. 7. After denoising, the margin of cross-sections of blood vessel became smooth and SNR of image was improved, which was of great benefit to obtain the clear blood vessel images in 3D reconstruction. As shown in Fig. 8(A), the denoised 2D OCT images were stacked to 3D OCT images using Amira. To further analyze the effect of PEG-GNRs on OCT imaging of cerebral blood vessels at different time points, selected ROIs were magnified, as shown in Fig. 8(B). Here, contrast enhancement (CE) was defined according to Eq. (4) (where API indicates average pixel intensity)[18,30];

$$CE(dB) = 10\log_{10}\frac{API \text{ of } ROI \text{ (with PEG-GNRs)}}{API \text{ of } ROI \text{ (without PEG-GNRs)}}. \tag{4}$$

The OCT signal intensity and contrast enhancement in ROIs were calculated and plotted to curves, as shown in Fig. 8(C). After the injection of PEG-GNRs, more tiny blood vessels can be detected and the OCT signal gradually increased over time, reaching a peak at 20 min. At this time, the contrast of OCT signal was enhanced by 5.87 dB. The smaller regions of blood vessels can be seen visually.

The enhancement then declined gradually for 60 min. These results indicated that the microcirculation of the cerebral blood vessels in mouse could be clearly reflected by the OCT, this would be of great help to the brain disease diagnosis and therapeutic drug monitoring. These results also indicated a dynamic change in the effect of PEG-GNRs in brain blood vessels of mice, supporting the use of PEG-GNRs, which possessed strong scattering wavelength ability, for enhancing the signal intensity and contrast in OCT imaging.

In addition, 3 h after the craniotomy, the mouse's physiological status was weaker due to the low temperature of the experimental environment and trauma caused by craniotomy, and the OCT imaging of cerebral blood vessels was performed, as shown in Fig. 9(a). Obviously, the vascular image was very blurred. To further analyze the cause of angiography at this time, compare it with the mouse angiography in normal state [without injection of PEG-GNRs, Fig. 9(b)] and the ROIs were selected for OCT signal intensity fitting, as shown in Fig. 9(c). When the mouse was in a weak state of life, it can be seen that most of blood vessels were lost, except for some of the larger blood vessels [the parts were marked by white dashed line in the corresponding Figs. 9(a) and 9(b)], and the OCT signal intensity was reduced by nearly 40%. Combining the OCT imaging principle and signal intensity changes of blood vessels in different states,[34,35] it can be known that the OCT signal of blood vessel imaging mainly comes from the scattering of blood. The reduction of scattering and decrease of OCT signal intensity were mainly due to lesser blood volume and slower blood flow, therefore we can judge that mouse was currently in a state of brain ischemia based on this phenomenon. Hence,
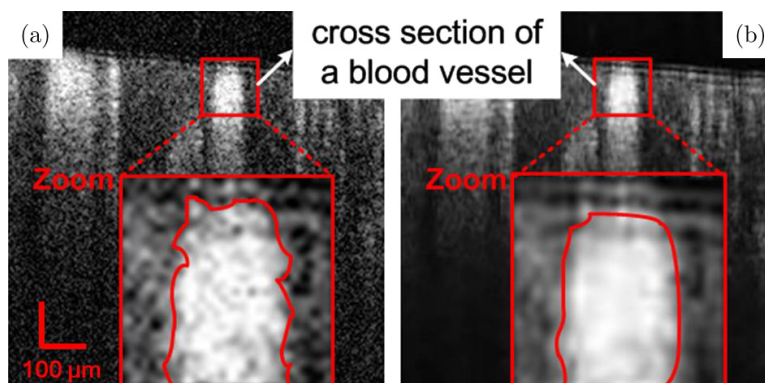

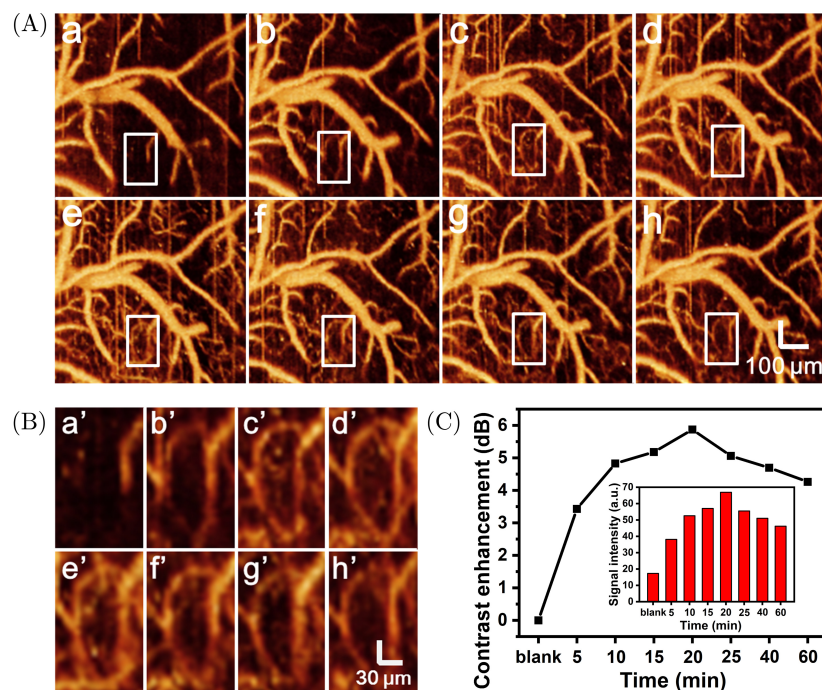Fig. 7.   2D OCT images of blood vessels (a) before and (b) after denoising by BM3D.

Fig. 8.   (A) 3D OCT images of cerebral blood vessels in mice in the absence (a) and presence of PEG-GNRs (1 nM) at various time points, i.e., (b) 5, (c) 10, (d) 15, (e) 20 (f) 25, (g) 40 and (h) 60 min; (B) Magnified images of representative blood vessels marked with white solid rectangles in (A); (C) Curve of the contrast enhancement of ROIs corresponding to (B); The inset showed the OCT signal intensity for (B).
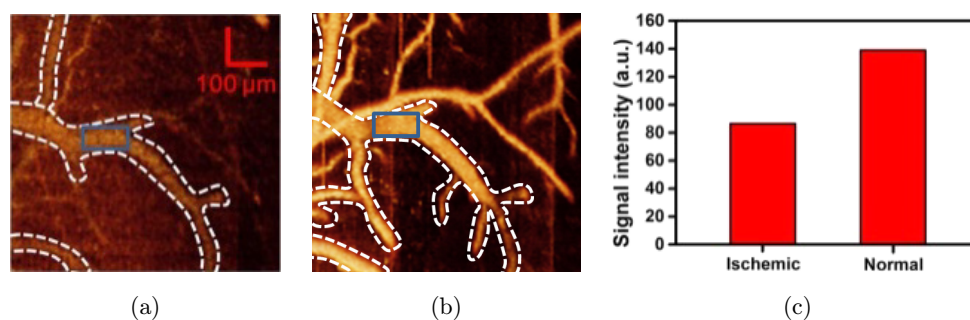

Fig. 9.   3D OCT images of (a) ischemic and (b) normal cerebral blood vessels in mice; (c) OCT signal intensity of ROIs which were marked with blue solid rectangles in (a) and (b).

the results proved that SD-OCT can be used as a research tool for brain disease diagnosis.

5.   Conclusion

In summary, PEG-GNRs had high scattering and therefore was suitable contrast agents for OCT imaging. By the contrast-enhanced SD-OCT, more tiny blood vessels can be detected *in vivo* and the image contrast was improved by 5.87 dB, simultaneously monitoring the dynamic changes of PEG-GNRs in blood vessels in mice. Besides, based on the sensitivity of the signal to blood changes during OCT imaging, we obtained brain vascular changes in both normal and ischemic conditions in mouse. These results revealed that OCT assisted by contrast agent not only can obtain clear distribution of cerebral blood vessels, but also can be applied to the further research of brain microcirculation functional imaging and cerebral ischemia monitoring, which are of great significance to disease diagnosis, research and therapeutic drug monitoring for cerebral vascular diseases.

Ethical Statement

All the mice used were purchased from Guangdong Medical Laboratory Animal Center. Additionally, all animal procedures were performed in strict compliance with the requirements and guidelines of the Laboratory and Equipment Department and Institutional Ethical Committee of Animal Experimentation of Health Science Center, Shenzhen University.

Conflict of Interest

We declare that the authors have no competing interests as defined by Journal of Innovative Optical Health Science, or other interests that might be perceived to influence the results and discussion reported in this paper.

Acknowledgments

References

1. Y. Kolinko, K. Krakorova, J. Cendelin, Z. Tonar, M. Kralickova, "Microcirculation of the brain: Morphological assessment in degenerative diseases and restoration processes," *Rev. Neurosci.* **26**(1), 75–93 (2015).

2. J. I. Friedman, C. Y. Tang, H. J. de Haas, L. Changchien, G. Goliasch, P. Dabas, V. Wang, Z. A. Fayad, V. Fuster, J. Narula, "Brain imaging changes associated with risk factors for cardiovascular and cerebrovascular disease in asymptomatic patients," *Jacc-Cardiovasc Imag.* **7**(10), 1039–1053 (2014).

3. Y. Satomura, J. Seki, Y. Ooi, T. Yanagida, A. Seiyama, "*In vivo* imaging of the rat cerebral microvessels with optical coherence tomography," *Clinical Hemorheol. Microcircul.* **31**(1), 31–40 (2004).

4. J. Seki, Y. Satomura, Y. Ooi, T. Yanagida, A. Seiyama, "Velocity profiles in the rat cerebral microvessels measured by optical coherence tomography," *Clin Hemorheol Microcirc.* **34**(34), 233–239 (2006).

5. O. A. Izotova, A. L. Kalyanov, V. V. Lychagov, O. V. Semyachkina-Glushkovskaya, "Correlation mapping method of OCT for visualization blood vessels in brain," *Proc. of SPIE.* **9032**, 90320G (2013).

6. M. S. Mathews, J. Su, E. Heidari, E. I. Levy, M. E. Linskey, Z. Chen, "Neuroendovascular optical coherence tomography imaging and histological analysis," *Neurosurgery.* **69**(2), 430–439 (2011).

7. C. Xu, J. Ye, D. L. Marks, S. A. Boppart, "Near-infrared dyes as contrast-enhancing agents for spectroscopic optical coherence tomography," *Opt. Lett.* **29**(14), 1647–1649 (2004).

8. C. Yang, M. A. Choma, L. E. Lamb, J. D. Simon, J. A. Izatt, "Protein-based molecular contrast optical coherence tomography with phytochrome as the contrast agent," *Opt. Lett.* **29**(12), 1396–1398 (2004).

9. Y. Ponce de León, J. L. Pichardo-Molina, N. Alcal'a Ochoa, D. Luna-Moreno, "Contrast enhancement of optical coherence tomography images using branched gold nanoparticles," *J. Nanomater.* **11**(25), 128 (2012).

10. H. Y. Tseng, C. K. Lee, S. Y. Wu, T. T. Chi, K. M. Yang, J. Y. Wang, Y. W. Kiang, C. C. Yang, M. T. Tsai, Y. C. Wu, H. Y. E. Chou, C. P. Chiang, "Au nanorings for enhancing absorption and backscattering monitored with optical coherence tomography," *Nanotechnol.* **21**(29), 295102 (2010).

11. Y. Pan, J. You, N. D. Volkow, K. Park, C. Du, "Ultrasensitive detection of 3D cerebral microvascular network dynamics *in vivo*," *NeuroImage.* **103**, 492–501 (2014).

12. O. Liba, E. D. SoRelle, D. Sen, A. de la Zerda, "Contrast-enhanced optical coherence tomography with picomolar sensitivity for functional *in vivo* imaging," *Sci. Rep.* **6**, 23337 (2016).

13. J. C. Kah, M. Olivo, T. H. Chow, K. S. Song, K. Z. Koh, S. Mhaisalkar, C. J. Sheppard, "Control of optical contrast using gold nanoshells for optical coherence tomography imaging of mouse xenograft tumor model *in vivo*," *J. Biomed. Opt.* **14**(5), 054015 (2009).

14. J. Zhang, J. Liu, L. Wang, Z. Li, Z. Yuan, "Retroreflective-type Janus microspheres as a novel contrast agent for enhanced optical coherence tomography," *J. Biophotonics.* **10**(6–7), 878–886 (2017).

15. H. Assadi, V. Demidov, R. Karshafian, A. Douplik, I. Vitkin, "Microvascular contrast enhancement in

optical coherence tomography using microbubbles," *J. Biomed. Opt.* **21**(7), 76014 (2016).

16. X. Huang, S. Neretina, M. A. Elsayed, "Gold nanorods: From synthesis and properties to biological and biomedical applications," *Adv. Mater.* **21**(48), 4880–4910 (2009).

17. H. Chen, L. Shao, Q. Li, J. Wang, "Gold nanorods and their plasmonic properties," *Chem. Soc. Rev.* **42**(7), 2679–2724 (2013).

18. T. S. Troutman, J. K. Barton, M. Romanowski, "Optical coherence tomography with plasmon resonant nanorods of gold," *Opt. Lett.* **32**(11), 1438–1440 (2007).

19. D. Sen, E. D. Sorelle, O. Liba, R. Dalal, Y. M. Paulus, T. W. Kim, D. M. Moshfeghi, A. de la Zerda, "High-resolution contrast-enhanced optical coherence tomography in mice retinae," *J. Biomed. Opt.* **21**(6), 66002 (2016).

20. Y. Winetraub, E. D. Sorelle, O. Liba, A. de la Zerda, "Quantitative contrast-enhanced optical coherence tomography," *Appl. Phys. Lett.* **108**(2), 023702 (2016).

21. X. Jiang, R. Liu, P. Tang, W. Li, H. Zhong, Z. Zhou, J. Zhou, "Controllably tuning the near-infrared plasmonic modes of gold nanoplates for enhanced optical coherence imaging and photothermal therapy," *Rsc. Adv.* **5**(98), 80709–80718 (2015).

22. A. Lee, G. F. Andrade, A. Ahmed, M. L. Souza, N. Coombs, E. Tumarkin, K. Liu, R. Gordon, A. G. Brolo, E. Kumacheva, "Probing dynamic generation of hot-spots in self-assembled chains of gold nanorods by surface-enhanced Raman scattering," *J. Am. Chem. Soc.* **133**(19), 7563–7570 (2011).

23. K. Liu, C. Resetco, E. Kumacheva, "Salt-mediated kinetics of the self-assembly of gold nanorods end-tethered with polymer ligands," *Nanoscale.* **4**(20), 6574–6580 (2012).

24. P. Nezhad-Mokhtari, N. Arsalani, M. Ghorbani, H. Hamishehkar, "Development of biocompatible fluorescent gelatin nanocarriers for cell imaging and anticancer drug targeting," *J. Mater. Sci.* **53**(15), 10679–10691 (2018).

25. D. F. Kohn, S. K. Wixson, W. J. White, G. J. Benson, "Anesthesia and Analgesia in Laboratory Animals," *Can. Vet. J.* **39**(5), 304 (1997).

26. J. Gao, X. Peng, P. Li, Z. Ding, J. Qu, "Vascular distribution imaging of dorsal skin window chamber in mouse with spectral domain optical coherence tomography," *Front. Optoelectron.* **8**(2), 170–176 (2015).

27. X. Peng, S. Yang, B. Yu, Q. Wang, D. Lin, J. Gao, P. Zhang, Y. Ma, J. Qu, H. Niu, "Continuous imaging of the blood vessels in tumor mouse dorsal skin window chamber model by using SD-OCT," *Proc. SPIE* 96973N (2016).

28. S. Yang, H. Chen, L. Liu, B. Chen, Z. Yang, C. Wu, S. Hu, H. Lin, B. Li, J. Qu, "OCT imaging detection of brain blood vessels in mouse, based on semiconducting polymer nanoparticles," *Analyst.* **142**(23), 4503–4510 (2017).

29. T. C. Chen, B. Cense, M. C. Pierce, N. Nassif, B. H. Park, S. H. Yun, B. R. White, B. E. Bouma, G. J. Tearney, J. F. de Boer, "Spectral domain optical coherence tomography: Ultra-high speed, ultra-high resolution ophthalmic imaging," *Arch. Ophthalmol.* **123**(12), 1715–1720 (2005).

30. Y. P. De León, J. L. Pichardo-Molina, N. A. Ochoa, D. Luna-Moreno, "Contrast enhancement of optical coherence tomography images using branched gold nanoparticles," *J. Nanomater.* **11**, 128 (2012).

31. K. M. Ratheesh, P. Prabhathan, L. K. Seah, V. M. Murukeshan, "Gold nanorods with higher aspect ratio as potential contrast agent in optical coherence tomography and for photothermal applications around 1300 nm imaging window," *Biomed. Phys. Eng. Express.* **2**(5), 055005 (2016).

32. M. Zhang, L. Lin, "Enhancement of coherent optical signal from tissue phantom by gold nanorods in near-infrared range," *Optik — Int. J. Light Electron Opt.* **127**(20), 8983–8987 (2016).

33. B. Chong, Y. K. Zhu, "Speckle reduction in optical coherence tomography images of human finger skin by wavelet modified BM3D filter," *Opt. Commun.* **291**(6), 461–469 (2013).

34. D. H. Tycko, M. H. Metz, E. A. Epstein, A. Grinbaum, "Flow-cytometric light scattering measurement of red blood cell volume and hemoglobin concentration," *Appl. Opt.* **24**(9), 1355 (19851).

35. J. Mauer, M. Peltomaki, S. Poblete, G. Gompper, D. A. Fedosov, "Static and dynamic light scattering by red blood cells: A numerical study," *Plos One.* **12**(5), e0176799 (2017).